Delft University of Technology

Theoretical minimum uncertainty of single-molecule localizations using a single-photon avalanche diode array

Houwink, Quint; Kalisvaart, Dylan; Hung, Shih Te; Cnossen, Jelmer; Fan, Daniel; Mos, Paul; Ülkü, Arin Can; Bruschini, Claudio; Charbon, Edoardo; Smith, Carlas S.

Important note
To cite this publication, please use the final published version (if applicable).
Please check the document version above.

Theoretical minimum uncertainty of single-molecule localizations using a single-photon avalanche diode array

QUINT HOUWINK,[1] DYLAN KALISVAART,[1] ⓘ SHIH-TE HUNG,[1]
JELMER CNOSSEN,[1] DANIEL FAN,[1] PAUL MOS,[2] ARIN CAN ÜLKÜ,[2]
CLAUDIO BRUSCHINI,[2] ⓘ EDOARDO CHARBON,[2] AND CARLAS S.
SMITH[1],* ⓘ

[1]*Delft Center for Systems and Control, Delft University of Technology, Delft, The Netherlands*
[2]*Advanced Quantum Architecture Lab, EPFL, Neuchâtel, Switzerland*
*c.s.smith@tudelft.nl

Abstract: Single-photon avalanche diode (SPAD) arrays can be used for single-molecule localization microscopy (SMLM) because of their high frame rate and lack of readout noise. SPAD arrays have a binary frame output, which means photon arrivals should be described as a binomial process rather than a Poissonian process. Consequentially, the theoretical minimum uncertainty of the localizations is not accurately predicted by the Poissonian Cramér-Rao lower bound (CRLB). Here, we derive a binomial CRLB and benchmark it using simulated and experimental data. We show that if the expected photon count is larger than one for all pixels within one standard deviation of a Gaussian point spread function, the binomial CRLB gives a 46% higher theoretical uncertainty than the Poissonian CRLB. For typical SMLM photon fluxes, where no saturation occurs, the binomial CRLB predicts the same uncertainty as the Poissonian CRLB. Therefore, the binomial CRLB can be used to predict and benchmark localization uncertainty for SMLM with SPAD arrays for all practical emitter intensities.

1. Introduction

Single-photon avalanche diode (SPAD) arrays are image detectors capable of detecting single photons at a rate of 100 kfps [1]. SPAD arrays are used for single-molecule localization microscopy (SMLM) [2–5], single-molecule tracking [6], and fluorescence lifetime imaging microscopy (FLIM) [7–9]. SPAD arrays lack readout noise, giving them an advantage over sCMOS cameras. Individual SPADs are also able to time-stamp photons with picosecond precision, which makes them viable options for time-of-flight (ToF) imaging [10,11].

A key feature of a SPAD array is its output of binary frames. A number of frames is aggregated into an image to create contrast. The binary output is because SPADs work with a reverse-biased p-n junction that is ultra-sensitive to incident photons. A photon triggers an avalanche in the junction, which causes a current that can be measured. After the avalanche, the SPAD has to recharge beyond its breakdown voltage. During this recharging the SPAD is insensitive to incident photons as shown in Fig. (1(b)). Some SPADs are capable of measuring photons during recharging, but this requires the SPAD to store the counts in a pixel memory, which lowers the fill factor of a SPAD array. Therefore, we focus on SPADs that measure one photon maximum per detection cycle, giving a binary output [12].

A fundamental problem in SMLM is determining and achieving the optimal precision with which single molecules are localized. The theoretical minimum uncertainty can be calculated using the Cramér-Rao lower bound (CRLB). The CRLB holds for an unbiased parameter estimation problem such as maximum likelihood estimation (MLE), which is asymptotically unbiased [13]. The CRLB is dependent on the image formation model. In the derivation of an
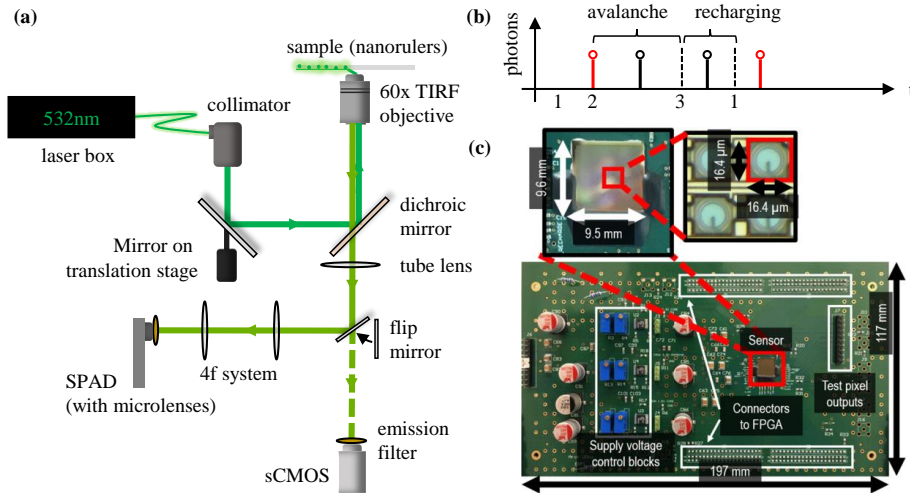
Fig. 1. Experimental method for single-molecule localization using a SPAD array. (**a**) The TIRF setup used for the experimental data in this paper. A green laser (532 nm) is directed towards an objective such that it enters the sample at a critical angle, only exciting the nanorulers close to the coverslip. The emitted light is filtered from the excitation light using a dichroic mirror and magnified 2.7× by a 4f system before being focused on the 512×256 SPAD array using microlenses. An sCMOS camera was used to find the focal plane and for imaging comparison. (**b**) A schematic of photon arrivals on the SPAD. The SPAD is charged beyond its breakdown voltage at 1. An incident photon at 2 then triggers an avalanche. The SPAD is then recharged at point 3. No photons are detected between 2 and 1, causing the binary behavior of the SPAD. (**c**) The SwissSPAD2, consisting of 512×256 active pixels. The pixels have a pitch of 16.38μm, and a low fill factor of 10.5% that was increased to 50% using microlenses.

image formation model for SMLM with negligible readout noise, the photon count is modelled as a Poisson process [14]. The Poisson process accounts for the discrete nature of photon arrivals.

Using a Poisson distribution to calculate the CRLB for SMLM with a SPAD array is inaccurate as the SPAD array is unable to register more than one photon per exposure time period. Therefore, if saturation occurs, there is no guarantee that a Poissonian CRLB derived by [13] holds for experiments using a SPAD array. We consider a region of interest around an emitter to be saturated if the expected photon count is larger than one in all pixels within one standard deviation of a point spread function. Research into performing SMLM with SPAD arrays [2,6,15] has refrained from using a CRLB. Therefore, applied SMLM methods cannot be benchmarked to a theoretical minimum uncertainty.

Here, we derive the CRLB for SMLM applications when using a SPAD array. The output of the SPAD array is modelled as a binomial distribution, thereby creating a physically accurate representation of aggregating multiple binary SPAD array images. Additionally, we incorporate a pixel-dependent dark count rate (DCR) in the estimation algorithm and CRLB. We validate this model using simulations and empirical data. In these experiments we show that, if saturation occurs, the binomial CRLB gives a higher theoretical uncertainty than the Poissonian CRLB. Without saturation, the binomial CRLB predicts the same uncertainty as the Poissonian CRLB.

2. Methods and data

2.1. Maximum likelihood estimation for a single-photon avalanche diode array

We use the maximum likelihood principle to obtain an estimate of the molecule position. For the derivation of the image formation model needed to calculate the likelihood, molecules are assumed to be excited by a uniform laser light and have a Gaussian point spread function [16]. This point spread function is summed with any background noise and discretized over the finite size of the pixels of the SPAD. This yields the photon rate $\mu_k(\vec{\theta})$ in pixel k. $\vec{\theta}$ is the parameter vector containing the emitter position, intensity, and the background intensity. $\mu_k(\vec{\theta})$ is thereafter referred to as μ_k. To account for the discrete nature of light, the photon arrivals are modelled as a Poisson process with a rate equal to the expected photon count. This does not yet take the binary behavior of the SPAD or SPAD particular noise into account.

The dark count rate (DCR) is a noise that is particular to SPADs. The DCR is caused by spontaneous avalanches within the SPAD and can be modelled as a Poisson process over time [17]. As some SPADs in the array are highly vulnerable to DCR (10-100 times higher than the median DCR), the DCR is pixel-dependent (see Supplement 1) and constant over time (see Supplement 1). DCR_k is calculated for each pixel k by measuring the average dark counts per frame and accounting for the binary behavior using a logarithmic correction formula (see Supplement 1). We sum the average DCR with the incident photon rate to obtain the expected photon rate. Equation (1) shows the probability mass function of the photon detections if the SPAD array output would be discrete. Here, c_k is the photon count in pixel k and t_e is the exposure time.

$$\mathbb{P}(C_k = c_k) = \frac{t_e \left(\mu_k + DCR_k\right)^{c_k} e^{-t_e(\mu_k + DCR_k)}}{c_k!} \tag{1}$$

The SPAD has a binary output, therefore we sum the probabilities of observing more than zero photons in one frame to get the probability of observing one photon. This probability is equal to one minus the probability of observing zero photons, i.e. $c_k = 0$. This transforms the Poisson distribution into a Bernoulli distribution. The photon arrivals in a pixel thus follow a binomial distribution when aggregating multiple binary frames. The likelihood of an observed image $\vec{c}_N$ with n pixels is computed in Eq. (2), where $c_{N,k}$ is the number of photons in pixel k, upon aggregating N frames. It is assumed that there is no correlation between pixels, i.e. no crosstalk [18]. Equation (2) can be maximized to obtain a parameter estimate. We use the Levenberg-Marquardt algorithm to maximize the likelihood (see Supplement 1). Note that the average DCR is incorporated into the maximum likelihood as a constant as opposed to subtracting it from the observed photon counts prior to the maximum likelihood estimation. In doing so, we prevent potentially negative values in $c_{N,k}$, which would cause numerical issues.

$$L(\vec{\theta}|\vec{c}_N) = \prod_{k=1}^{n} \binom{N}{c_{N,k}} (1 - e^{-t_e(\mu_k + DCR_k)})^{c_{N,k}} e^{-t_e(\mu_k + DCR_k)(N - c_{N,k})} \tag{2}$$

2.2. Cramér-Rao lower bound for a single-photon avalanche diode array

The CRLB gives the lowest possible uncertainty of the position of a molecule, given an image formation model [13]. There are two main applications for the CRLB. First, it provides a bound on the achievable resolution of an experiment beforehand, which can be used to design the experiment. Second, it can be used to benchmark a particular localization approach. The CRLB holds for unbiased estimators and is defined as the entries on the diagonal, i.e. $i = j$, of the inverse of the Fisher information matrix [19]. Using the likelihood function in Eq. (2), the Fisher

information matrix for the binomial CRLB is given in Eq. (3) (see Supplement 1).

$$I_{i,j}\left(\vec{\theta}\right) = Nt_{\mathrm{e}}^2 \sum_{k=1}^{n} \left(\frac{\partial \mu_k}{\partial \theta_i} \frac{\partial \mu_k}{\partial \theta_j} \frac{e^{-t_{\mathrm{e}}(\mu_k + \mathrm{DCR}_k)}}{1 - e^{-t_{\mathrm{e}}(\mu_k + \mathrm{DCR}_k)}} \right)$$

$$\mathrm{CRLB}\left(\vec{\theta}\right) = I(\vec{\theta})^{-1}$$

(3)

2.3. Simulation method

We performed simulations of emitter imaging at intensities where no saturation occurs (all pixels have less than 1 expected photon per pixel) up to the point where heavy saturation occurs (4 expected photons for the center pixels). This gives a broad scope of the behavior of the achieved and theoretical uncertainty when acquiring SMLM images using a SPAD array. Blinking behavior of the emitters was neglected to have a constant intensity over the localizations. The background intensity was kept constant for each frame in one simulation and at 3% of the emitter intensity in another simulation.

The simulated frames are obtained using a Gaussian distribution for the point spread function of a single emitter. The point spread function is given a standard deviation of 102 nm, which is equal to the point spread function of the emitters in the experimental setup. The intensity is varied over a range of photon counts, from 90 to 22,000 photons per emitter per image. DCR is simulated using experimental SwissSPAD2 data acquired in a dark environment. Each frame is made binary by first applying a Poissonian distribution on the calculated intensity for a pixel and then setting all pixels with a value above one to one. Subsequently, N frames are aggregated to get an image with a total exposure time of $N \times t_{\mathrm{e}}$.

Maximum likelihood estimation described in Section 2.1 estimates the optimal position and intensity of the emitter, as well as the background intensity. Each intensity simulation is repeated 500 times. A Gaussian distribution is fitted on the x-coordinate and y-coordinate of the estimated positions to obtain the standard deviation σ_x and σ_y, which is the uncertainty of the emitter position.

2.4. Empirical method

An experimental setup was built to validate the proposed CRLB model. The used SPAD array is the SwissSPAD2, shown in Fig. (1(c)). The SwissSPAD2 has an active array of 512×256 pixels with a pitch of 16.38 μm. It has a photon detection probability of 45% at 562 nm and a fill factor of 10.5%. The fill factor is increased to approximately 50% for this experiment through the use of microlenses [20]. For this experiment the SwissSPAD2 is operated at an excess bias of 6.5V. The SPAD array is connected to a field-programmable gate array (Opal Kelly XEM7360), which is programmed with the imaging mode and handles the live data transfer via USB 3.0.

The SMLM setup used is a total internal reflection fluorescence (TIRF) microscope. A diagram of the setup is shown in Fig. (1(a)). A 200 mW, 532 nm continuous-wave laser (Optoelelectronics Tech. PSU-H-LED) is collimated and directed to a 60x objective (Olympus Apo N 60x/1.49Oil) where it arrives off-center such that the light is deflected along the surface of the sample. The beam can be moved further from or closer to the center using a mirror and a lens on a translation stage. This causes only a fraction of the fluorophores, i.e. those close to the coverslip, to emit photons, reducing the background noise. A dichroic mirror (Semrock, Di01-R405/488/532/635-25x36) filters the emitted light from the sample prior to the tube lens (ThorLabs, AC508-180-AL-M). A flip mirror (ThorLabs, TRF90/M) switches between an sCMOS camera (ANDOR Zyla 4.2) for comparison and the SwissSPAD2. As the sCMOS camera has a pixel pitch of 6.5μm, a 4f system (ThorLabs, AC508-075-AL-M and AC508-200-AL-M) with magnification 2.7x is added to the SPAD trajectory. Consequentially, the SPAD array has a point spread function with a standard deviation of 102 nm, equal to that imaged by the sCMOS camera. A quadband filter (Semrock,

390/482/532/640 HC) on the imagers filters the remaining excitation light. DNA-Paint nanorulers (Gattaquant PAINT 80RG) are used as the sample. The nanorulers consist of three binding sites seperated linearly by 80 nm between each site. Fluorophores (ATTO542 and ATTO655) connect to the binding sites for a varying amount of time until releasing again. This results in blinking and thus sparse emitters which are capable of being localized using SMLM algorithms. The 532 nm laser source excites only the ATTO542 fluorophores, which emit light of wavelength 562 nm. At this wavelenght the SwissSPAD2 is most sensitive for incident photons (see Supplement 1).

Experimental data is gathered at an exposure time of 15 μs. At this rate, the maximum field of view is 128x256 pixels. These frames are then summed to create frames with exposure times between 15 μs and 1.9 ms. Any pixel with a value above one is set to one. The frames are then aggregated to create a total exposure time per image of 31 ms using a varying number of aggregated frames N. N ranges from 16 to 2048 frames in 8 steps. At this total exposure time the expected emitter intensity is approximately 650 photons per image. The SwissSPAD2 used for this paper experiences a higher DCR in one corner (see Supplement 1). Therefore, the opposite quarter of the SPAD array was used for the nanoruler localizations (see Supplement 1). Regions of interest (ROIs) are then identified in each image by placing a threshold on a Gaussian ($\sigma = \sigma_{\mathrm{PSF}}$) filtered image [21]. Estimates are obtained by maximizing the likelihood given in Eq. (2). Many estimates do not represent an emitter, but dust on the sample or a cluster of hot pixels. To filter these estimates, the χ^2 value was calculated for an estimate and filtered above a threshold (see Supplement 1). Additionally, only the localizations belonging to a nanoruler were used to filter out any fluorophores floating into the focal plane without binding (see Supplement 1). Any drift in the estimates is removed using the redundant cross-correlation tool provided by Picasso [22]. Finally, the estimates are clustered when they are within three times the expected uncertainty from one another and not more than five frames apart [14]. Each cluster is fit with a Gaussian distribution. The mean and standard deviation of the fitted distribution yield the final emitter position and uncertainty, respectively.

3. Results

3.1. Simulated results

An emitter was simulated at 25 intensities, equidistantly spaced within $\left[10^2, 10^4\right]$ photons per image. This was repeated for 255, 510 and 1275 aggregated frames per image. Figure (2) shows the achieved uncertainty for the localization of this emitter as well as the theorized minimum uncertainty calculated using the binomial and Poissonian CRLB. The intensity range was selected such that a distinction can be made between the uncertainty theorized by both CRLB models. Figure (2(a)) shows a constant background rate of 2.5 photons per pixel in each frame. At this rate, almost no saturation occurs, which causes the binomial and Poissonian CRLB to be overlapping for almost all intensities. The CRLB models start deviating notably at emitter intensities above 4000 photons per image, as is shown in the zoom in Fig. (2(b)). In this plot it becomes clear that the binomial maximum likelihood estimator obtains the theoretical minimum uncertainty given the data.

An additional simulation was performed while keeping the background intensity at 3% of the emitter intensity. The Poissonian CRLB is now identical for all aggregation numbers. It can be observed that the background contributes to the saturation and the difference between the CRLB models is apparent at more than 2000 emitter photons per image. The vertical lines indicate the point where saturation occurs for the different aggregation numbers. The theoretical minimum uncertainty of the binomial CRLB is 46% higher than the theoretical minimum uncertainty of the Poissonian model when saturation occurs. There is a fivefold difference between the binomial CRLB and Poissonian CRLB, for the maximum simulated intensity of 20,000 emitter photons per image. This occurs when there is heavy saturation in the simulated image due to more than five expected photons in the center pixels, as shown in Fig. (2(d)). Aggregating more frames
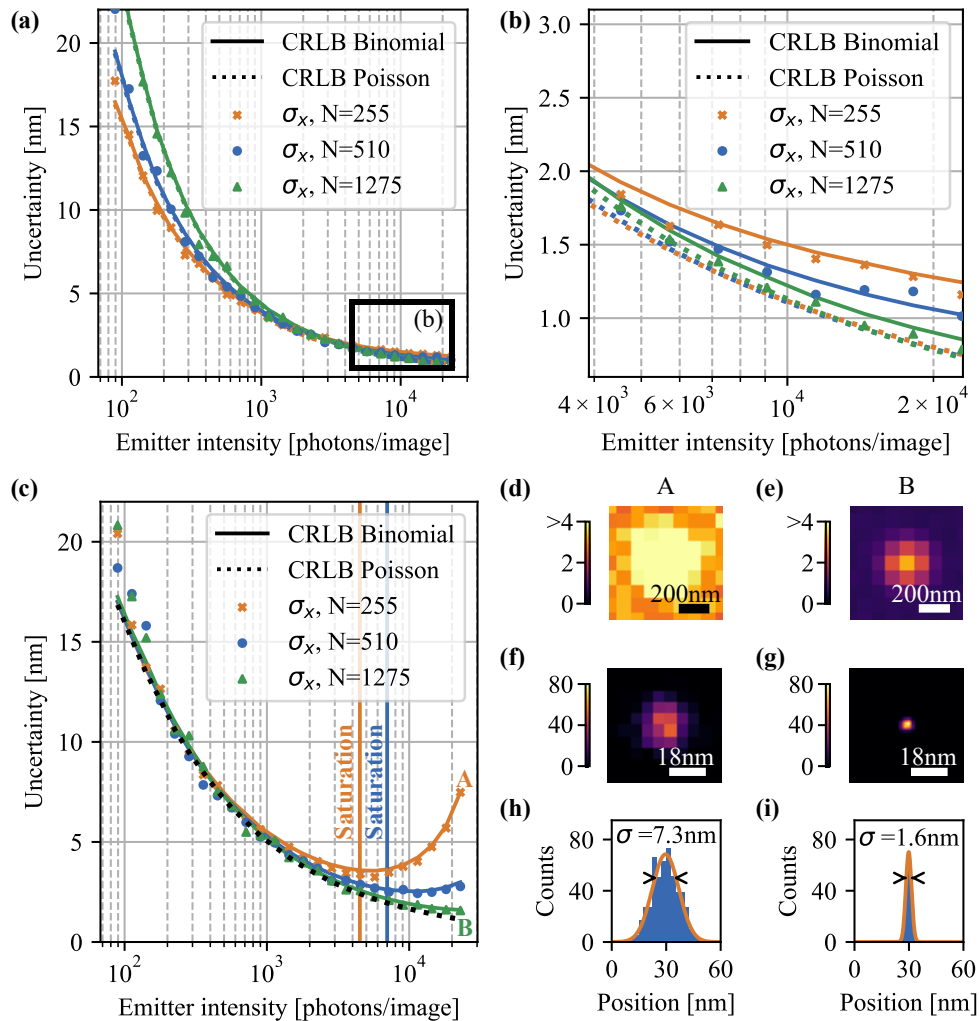
Fig. 2. Results of simulations at different intensities and aggregation. **(a)** Theorized and achieved uncertainty σ_x for simulated SPAD array images for different numbers of aggregated frames (N) and constant background of 2.5 photons per pixel. The binomial and Poissonian CRLB models are plotted, where the total exposure time is constant for each intensity . The binomial and Poissonian CRLB are identical for all lower intensities. **(b)** Zoom of the highest intensities in (a). At this point the binomial and Poissonian CRLB start deviating while the estimated uncertainties follow the binomial CRLB. **(c)** Same setting as (a), but with background noise equal to 3% of the emitter intensity, which causes the Poissonian CRLB to be identical for all aggregations. Points A and B show the effect of aggregating 255 frames versus 1275 frames. The vertical lines show the intensity where the expected photon count is larger than one for all pixels within one standard deviation of the Gaussian point spread function. No saturation occurs for 1275 aggregated frames. **(d-e)** Examples of one of the 500 simulated SPAD images of 255 and 1275 aggregated binary frames. The scale bar gives the expected number of photons per frame. In A, the exposure time per frame is five times higher than in B, resulting in more saturation. **(f-g)** 2D histograms of the 500 estimated positions based on simulated SPAD images for point A and B. The histograms resemble a 2D Gaussian distribution. **(h-i)** 1D histogram of the estimated positions. The standard deviation σ_x of the fitted Gaussian distribution is used as the uncertainty in plots (a-c).

lowers this difference as less saturation occurs. This is shown in Fig. (2(e)). Figures (2(f)) to (2(i)) are 2-dimensional and 1-dimensional histograms of the estimated positions for points A and B in Fig. (2(c)). These histograms show the effect of saturation on the estimated positions. The standard deviation of the estimated positions is five times higher for the frames in point A than in point B.

3.2. Empirical results

The empirical experiment was conducted at a constant total exposure time per image of 31 ms, varying the ratio between the number of frame aggregations and exposure time per frame. For this
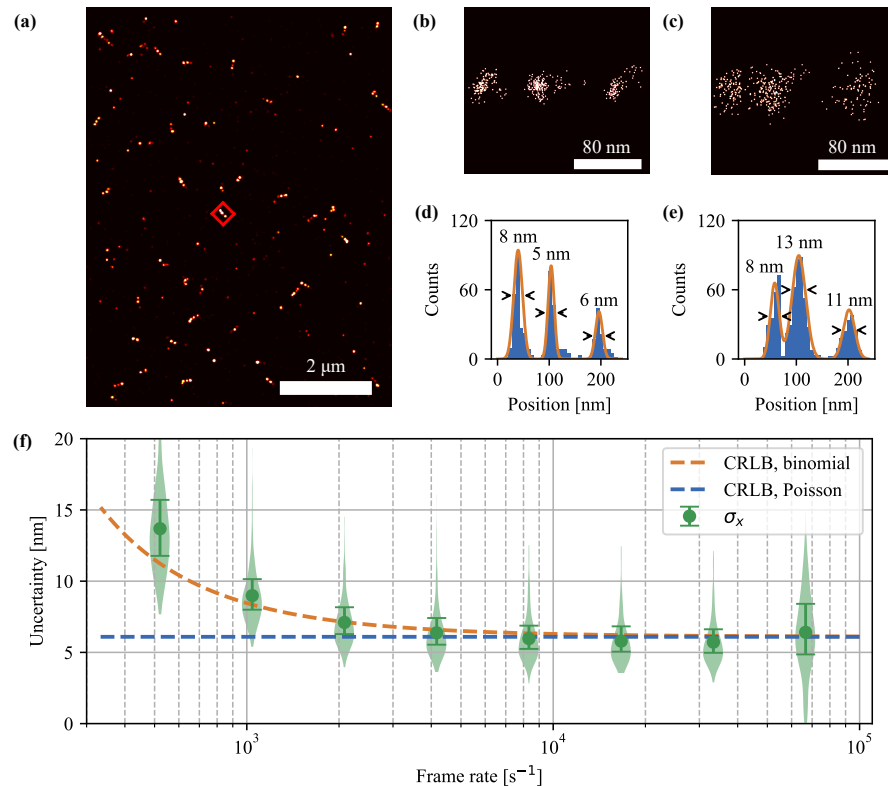

Fig. 3. Results of empirical experiment with the SwissSPAD2. **(a)** $10\mu m$ field of view of the SwissSPAD2 with 80 nm spaced nanorulers (see Supplement 1 for the complete field of view). For this field of view an exposure time of 15 μs was used and 2048 frames were aggregated. **(b)** Zoom in of (a) on one 80 nm spaced nanoruler with approximately 370 localizations. **(c)** The same nanoruler as in (b), but with an exposure time of 1.9 ms and 16 aggregated frames. **(d)** Localization histogram of the nanoruler in (b). The standard deviation of the Gaussian fits is the uncertainty σ_x. **(e)** Localization histogram of the nanoruler in (c). The standard deviation is higher than that in (d) and the localizations of the middle binding spot are biased towards the nearby left binding spot. **(f)** The achieved mean uncertainty for different frame rates and different aggregations, but a constant total exposure time of 31 ms. The theorized minimum uncertainty was plotted using the binomial and Poissonian model. The shaded area shows the distribution of the localization uncertainty and the error bars represent the first and fourth quarter. The CRLBs overlap at high frame rates and start differing below 128 aggregated frames. The SwissSPAD2 achieves the Cramér-Rao lower bound for all frame rates.

exposure time the average emitter intensity is 650 photons per image, which gives a theoretical minimum uncertainty of 6.5 nm for 2048 aggregated frames. Figure (3(f)) gives the achieved uncertainty for the localized emitters. The shaded area gives the density of the localization uncertainty with the vertical bars depicting the interquartile range. The spread in the achieved uncertainty is attributed to the different blinking durations of the emitters and thus different true intensities. The Poissonian and binomial CRLB are plotted to give the theoretical uncertainty. The two CRLBs start differing from one another below 4000 frames per second. A twofold difference in uncertainty was measured for 16 aggregated frames at a frame rate of 660 frames per second.

The sCMOS camera was used to benchmark the experimental results (see Supplement 1). The same experimental setup was used as described in Section 2.4. The used exposure time was set at 31 ms, equal to the total exposure time of the aggregated frames of the SPAD array. The sCMOS camera has a photon detection efficiency of 80%, which is 3.5 times higher than that of the SwissSPAD2. The SwissSPAD2 measured an average of 653 photons per image for each emitter. The sCMOS camera measured 1845 photons per image for each emitter (see Supplement 1). Consequentially, the average achieved uncertainty of the sCMOS camera was 3.7 nm.

4. Conclusions

SPAD arrays have a high frame rate but output binary frames. This fundamentally changes the image formation model used for SMLM applications, which assumes photon arrivals to follow a Poissonian distribution. The image formation model is used to calculate the theoretical minimum uncertainty that can be achieved in SMLM by calculating the CRLB [13]. Using the theoretical minimum uncertainty, it is possible to predict and benchmark the achieved uncertainty for a particular localization approach. Recent research into using SPAD arrays for SMLM [2,6,15] has not yet derived the theoretical minimum uncertainty when using a SPAD array. In this paper, we propose a binomial CRLB specifically for SMLM with a SPAD array.

We have shown that if saturation occurs, the theorized uncertainty of the binomial CRLB is 46% higher than the Poissonian CRLB. Saturation occurs if all pixels within one standard deviation of the point spread function have more than one expected photon arrival during one frame period. In simulations, individual pixels were saturated by modelling pixels up to four photon arrivals per frame period. For this case there was a factor five difference between the theorized uncertainty of the Poissonian CRLB and the proposed binomial CRLB, which was confirmed by the achieved uncertainty in the simulation.

Further investigation into this difference using empirical data demonstrated that saturation is unlikely to occur in SMLM. The difference between the Poissonian and binomial CRLB was limited to twofold for low frame rates and negligible for high frame rates, where no saturation occurred. Therefore, the binomial CRLB can be used to predict and benchmark localization uncertainty for SMLM with SPAD arrays for all practical intensities, but is especially relevant if saturation is present.

The empirical data in this research was limited by the photon detection efficiency of the SwissSPAD2 and nanoruler intensity. As a consequence, it was impossible to reproduce the fivefold difference between the binomial and Poissonian theoretical uncertainty in the empirical experiment. Thus the binomial CRLB will become more important as the photon detection probability of SPAD devices increases in the future.

A further study could assess the theoretical uncertainty of SPAD arrays in super-resolution methods other than SMLM. The high frame rate of the SPAD array can prove to be a valuable contribution to single-molecule tracking for instance. This method will benefit from the binomial CRLB when determining what exposure time to use in the trade-off between localization uncertainty and displacement due to Brownian motion. We also see applications for the findings of this study in time-of-flight imaging. This type of imaging is susceptible to pixel saturation

because of the unpredictable reflectivity of objects. It will therefore benefit from the binomial CRLB proposed in this paper by allowing researchers to benchmark their uncertainty to the theoretical minimum uncertainty.

Disclosures. For the sake of transparency, the authors would like to disclose that (i) Edoardo Charbon holds the position of Chief Scientific Officer of Fastree3D, a company making LiDARs for the automotive market, and that (ii) Claudio Bruschini and Edoardo Charbon are co-founders of Pi Imaging Technology. Both companies have not been involved with the paper drafting.

Data availability. The raw image data and processed localization data is available in Ref. [23]. The software and updates for simulating and processing SPAD datasets are available in Ref. [24].

Supplemental document. See Supplement 1 for supporting content.

References

1. S. Burri, F. Powolny, C. E. Bruschini, X. Michalet, F. Regazzoni, and E. Charbon, "A 65k pixel, 150k frames-per-second camera with global gating and micro-lenses suitable for fluorescence lifetime imaging," in *Optical Sensing and Detection III*, vol. 9141 F. Berghmans, A. G. Mignani, and P. D. Moor, eds., International Society for Optics and Photonics (SPIE, 2014), pp. 55–61.
2. I. Gyongy, A. Davies, N. A. W. Dutton, R. R. Duncan, C. Rickman, R. K. Henderson, and P. A. Dalgarno, "Smart-aggregation imaging for single molecule localisation with SPAD cameras," Sci. Rep. **6**(1), 37349 (2016).
3. I. M. Antolovic, S. Burri, C. Bruschini, R. Hoebe, and E. Charbon, "Nonuniformity analysis of a 65-kpixel cmos SPAD imager," IEEE Trans. Electron Devices **63**(1), 57–64 (2016).
4. V. Krishnaswami, C. J. F. Van Noorden, E. M. M. Manders, and R. A. Hoebe, "Towards digital photon counting cameras for single-molecule optical nanoscopy," Opt. Nano. **3**(1), 1 (2014).
5. I. Gyongy, A. Davies, B. Gallinet, N. A. Dutton, R. R. Duncan, C. Rickman, R. K. Henderson, and P. A. Dalgarno, "Cylindrical microlensing for enhanced collection efficiency of small pixel spad arrays in single-molecule localisation microscopy," Opt. Express **26**(3), 2280–2291 (2018).
6. I. Gyongy, A. Davies, A. M. Crespo, A. Green, N. A. W. Dutton, R. R. Duncan, C. Rickman, R. K. Henderson, and P. A. Dalgarno, "High-speed particle tracking in microscopy using SPAD image sensors," in *High-Speed Biomedical Imaging and Spectroscopy III: Toward Big Data Instrumentation and Management*, vol. 10505 K. K. Tsia and K. Goda, eds., International Society for Optics and Photonics (SPIE, 2018), pp. 29–34.
7. A. Ulku, A. Ardelean, M. Antolovic, S. Weiss, E. Charbon, C. Bruschini, and X. Michalet, "Wide-field time-gated SPAD imager for phasor-based FLIM applications," Methods Appl. Fluoresc. **8**(2), 024002 (2020).
8. H. A. R. Homulle, F. Powolny, P. L. Stegehuis, J. Dijkstra, D.-U. Li, K. Homicsko, D. Rimoldi, K. Muehlethaler, J. O. Prior, R. Sinisi, E. Dubikovskaya, E. Charbon, and C. Bruschini, "Compact solid-state cmos single-photon detector array for in vivo nir fluorescence lifetime oncology measurements," Biomed. Opt. Express **7**(5), 1797–1814 (2016).
9. C. Bruschini, H. Homulle, I. M. Antolovic, S. Burri, and E. Charbon, "Single-photon avalanche diode imagers in biophotonics: review and outlook," Light: Sci. Appl. **8**(1), 87 (2019).
10. K. Morimoto, A. Ardelean, M.-L. Wu, A. C. Ulku, I. M. Antolovic, C. Bruschini, and E. Charbon, "Megapixel time-gated SPAD image sensor for 2d and 3d imaging applications," Optica **7**(4), 346–354 (2020).
11. F. Heide, S. Diamond, D. B. Lindell, and G. Wetzstein, "Sub-picosecond photon-efficient 3d imaging using single-photon sensors," Sci. Rep. **8**(1), 17726 (2018).
12. F. Zappa, S. Tisa, A. Tosi, and S. Cova, "Principles and features of single-photon avalanche diode arrays," Sens. Actuators, A **140**(1), 103–112 (2007).
13. C. S. Smith, N. Joseph, B. Rieger, and K. A. Lidke, "Fast, single-molecule localization that achieves theoretically minimum uncertainty," Nat. Methods **7**(5), 373–375 (2010).
14. B. Rieger, R. Nieuwenhuizen, and S. Stallinga, "Image processing and analysis for single-molecule localization microscopy: Computation for nanoscale imaging," IEEE Signal Process. Mag. **32**(1), 49–57 (2015).
15. I. M. Antolovic, S. Burri, C. Bruschini, R. A. Hoebe, and E. Charbon, "SPAD imagers for super resolution localization microscopy enable analysis of fast fluorophore blinking," Sci. Rep. **7**(1), 44108 (2017).
16. B. Zhang, J. Zerubia, and J.-C. Olivo-Marin, "Gaussian approximations of fluorescence microscope point-spread function models," Appl. Opt. **46**(10), 1819 (2007).
17. A. Panglosse, P. Martin-Gonthier, O. Marcelot, C. Virmontois, O. Saint-Pe, and P. Magnan, "Dark count rate modeling in single-photon avalanche diodes," IEEE Trans. Circuits Syst. I **67**(5), 1507–1515 (2020).
18. I. Antolovic, "SPAD imagers for super resolution microscopy," Ph.D. thesis (2018).

19. S. M. Kay, *Fundamentals of Statistical Signal Processing: Estimation Theory* (Prentice-Hall, Inc., Upper Saddle River, NJ, USA, 1993).

20. A. C. Ulku, C. Bruschini, I. M. Antolovic, Y. Kuo, R. Ankri, S. Weiss, X. Michalet, and E. Charbon, "A 512 × 512 SPAD image sensor with integrated gating for widefield FLIM," IEEE J. Sel. Top. Quantum Electron. **25**(1), 1–12 (2019).

21. J. Cnossen, T. Hinsdale, R. Ø. Thorsen, M. Siemons, F. Schueder, R. Jungmann, C. S. Smith, B. Rieger, and S. Stallinga, "Localization microscopy at doubled precision with patterned illumination," Nat. Methods **17**(1), 59–63 (2020).

22. J. Schnitzbauer, M. T. Strauss, T. Schlichthaerle, F. Schueder, and R. Jungmann, "Super-resolution microscopy with dna-paint," Nat. Protoc. **12**(6), 1198–1228 (2017).

23. Q. Houwink, D. Kalisvaart, S.-T. Hung, J. Cnossen, D. Fan, P. Mos, A. C. Ülkü, C. Bruschini, E. Charbon, and C. Smith, "SwissSPAD2 images of nanorulers acquired using total internal reflection fluorescence microscopy," 4TU.ResearchData (2021), https://www.doi.org/10.4121/14975013.

24. Q. Houwink, D. Kalisvaart, S.-T. Hung, J. Cnossen, D. Fan, P. Mos, A. C. Ülkü, C. Bruschini, E. Charbon, and C. Smith, "Code for "Theoretical Minimum Uncertainty of Single-Molecule Localizations Using a Single-Photon Avalanche Diode Array"," Github (2021), https://github.com/qnano/spad_pipeline.